The Astrophysical Journal, 790:20 (11pp), 2014 July 20 doi:10.1088/0004-637X/790/1/20


# *SUZAKU* OBSERVATION OF THE BLACK HOLE BINARY 4U 1630–47 IN THE VERY HIGH STATE

Takafumi Hori[1], Yoshihiro Ueda[1], Megumi Shidatsu[1], Taiki Kawamuro[1], Aya Kubota[2], Chris Done[3], Satoshi Nakahira[4], Kohji Tsumura[5], Mai Shirahata[6,7], and Takahiro Nagayama[8]
[1] Department of Astronomy, Kyoto University, Kitashirakawa-Oiwake-cho, Sakyo-ku, Kyoto 606-8502, Japan; hori@kusastro.kyoto-u.ac.jp
[2] Department of Electronic Information Systems, Shibaura Institute of Technology, 307 Fukasaku, Minuma-ku, Saitama 337-8570, Japan
[3] Department of Physics, University of Durham, South Road, Durham, DH1 3LE, UK
[4] ISS Science Project Office, Institute of Space and Astronautical Science (ISAS), Japan Aerospace Exploration Agency (JAXA), 2-1-1 Sengen, Tsukuba, Ibaraki 305-8505, Japan
[5] Frontier Research Institute for Interdisciplinary Science, Tohoku University, Sendai, Miyagi 980-8578, Japan
[6] National Institutes of Natural Science National Astronomical Observatory of Japan (NAOJ) 2-21-1 Osawa, Mitaka, Tokyo 181-8588, Japan
[7] Department of Space Astronomy and Astrophysics, Institute of Space and Astronautical Science (ISAS), Japan Aerospace Exploration Agency (JAXA), Sagamihara, Kanagawa 252-5210, Japan
[8] Department of Physics, Faculty of Science, Kagoshima University, 1-21-35 Korimoto, Kagoshima, Kagoshima 890-0065, Japan
*Received 2014 January 24; accepted 2014 May 31; published 2014 June 27*

## ABSTRACT

We report the results from an X-ray and near-infrared observation of the Galactic black hole binary 4U 1630–47 in the very high state (VHS), performed with *Suzaku* and the Infrared Survey Facility around the peak of the 2012 September–October outburst. The X-ray spectrum is approximated by a steep power law, with photon index of 3.2, identifying the source as being in the VHS. A more detailed fit shows that the X-ray continuum is well described by a multicolor disk, together with thermal and nonthermal Comptonization. The inner disk appears slightly truncated by comparison with a previous high/soft state of this source, even taking into account energetic coupling between the disk and corona, although there are uncertainties due to the dust-scattering correction. The near-infrared fluxes are higher than the extrapolated disk model, showing that there is a contribution from irradiation in the outer disk and/or the companion star at these wavelengths. Our X-ray spectra do not show the Doppler-shifted iron emission lines indicating a baryonic jet that were seen four days previously in an *XMM-Newton* observation, despite the source being in a similar state. There are also no significant absorption lines from highly ionized iron lines as are seen in the previous high/soft state data. We show that the increased source luminosity is not enough on its own to make the wind so highly ionized as to be undetectable. This shows that the disk wind has changed in terms of its launch radius and/or density compared to the high/soft state.

*Key words:* accretion, accretion disks – black hole physics – stars: individual (4U 1630–47) – X-rays: binaries

*Online-only material:* color figures

## 1. INTRODUCTION

Galactic black hole binaries (BHBs) are ideal objects to study the physics of accretion flow onto a black hole. BHBs take several different states with distinct spectral and timing properties (for a review, see, e.g., Done et al. 2007). Generally, when the mass accretion rate (and hence the luminosity) is low, a BHB exhibits the low/hard state (LHS), where the spectrum is dominated by a power law with a photon index of $\Gamma \sim 1.7$ and a high-energy cutoff at $\sim$100 keV. At a higher mass accretion rate, the spectrum is dominated by optically thick, thermal emission from the accretion disk, which is well represented by the multicolor disk (MCD) model (Mitsuda et al. 1984; Makishima et al. 1986). This state is called the high/soft state (HSS). When the mass accretion rate becomes even larger and the luminosity is close to the Eddington limit, a BHB takes the so-called very high state (VHS), where the spectra are characterized by strong Comptonization. Although the VHS is a key state to understand the accretion disk physics under very high mass accretion rates, it has been rather poorly investigated because it is quite rare that a BHB takes this state.

The evolution of the state of a BHB during an outburst is complex and not solely determined by mass accretion rate. In typical outbursts, a BHB shows hysteresis with a q-shaped curve on a hardness–intensity diagram (e.g., Fender et al. 2004). Sources start from the LHS, then make a transition into the HSS, sometimes via the VHS. The source remains in the HSS while the luminosity declines, and then it turns back to the LHS, at a luminosity that can be a factor of 2–20 times smaller than the initial LHS-HSS transition. This hysteresis behavior probably originates from the accretion rate changing faster than the viscous timescale in the geometrically thin disk (Gladstone et al. 2007). However, BHBs in outbursts do not always exhibit similar evolutional tracks on this diagram (e.g., Nakahira et al. 2014), implying that the physical processes governing the spectral evolution in BHBs may be even more complicated.

An important issue in understanding black hole accretion flow in each state is whether the standard disk extends down to the innermost stable circular orbit (ISCO) around the black hole or is truncated at a larger radius. In the MCD model, the disk bolometric luminosity $L_{\rm disk}$ is related to the disk temperature $T_{\rm in}$ and innermost disk radius $r_{\rm in}$ as $L_{\rm disk} = 4\pi r_{\rm in}^2 \sigma T_{\rm in}^4$, where $\sigma$ is the Stefan–Boltzmann constant. The standard disk is believed to extend to the ISCO in the HSS, since the observed $r_{\rm in}$ value of a BHB is found to be constant over a wide range of $L_{\rm disk}$ (e.g., Ebisawa et al. 1993). By contrast, many studies suggest that the accretion disk in the LHS is truncated before reaching the ISCO (e.g., Makishima et al. 2008; Tomsick et al. 2009; Shidatsu et al. 2011, 2013) and the inner part is probably replaced by radiative inefficient accretion flow (e.g., Esin et al. 1997). The geometry of the innermost part of the accretion flow in the VHS is less clear, however. This is because in this state a hot corona might be strongly Compton-scattering photons emitted from the standard disk (Zdziarski et al. 2002; Gierliński & Done 2003;

Kubota & Done 2004), making it difficult to directly measure the intrinsic disk parameters. There are some reports that the innermost disk radius in the VHS is somewhat larger than that in the HSS (Kubota & Done 2004; Done & Kubota 2006; Tamura et al. 2012), indicating that the disk may be truncated before the ISCO. It is crucial to establish this picture by using high-quality broadband X-ray spectra of BHBs in the VHS.

4U 1630–47 is identified as a Galactic BHB because of the similarity of the spectral and temporal behaviors to other BHBs, although the mass of the compact object has not been measured yet. This object exhibits quasi-periodic outbursts with 600–700 day cycles. This period is very rapid as a BHB, probably indicating a high time-averaged mass accretion rate. The X-ray spectra of 4U 1630–47 are heavily absorbed ($N_{\rm H} \sim 8 \times 10^{22}$ cm$^{-2}$; Kubota et al. 2007), suggesting that the object is located near the Galactic center, although the accurate source distance $D$ is unknown. The nature of the companion has not been firmly identified yet; Augusteijn et al. (2001) infer that it may be an early-type star by assuming that the whole $K$-band magnitude in outburst comes from the companion.

Outbursts of 4U 1630–47 have been observed with many missions since the 1980s, including *EXOSAT* (Parmar et al. 1986), *Einstein/Ginga/ASCA* (Parmar et al. 1997), *BeppoSAX* (Oosterbroek et al. 1998), *RXTE* (e.g., Tomsick et al. 1998; Kuulkers et al. 1998; Tomsick & Kaaret 2000; Trudolyubov et al. 2001; Abe et al. 2005), *INTEGRAL* (Tomsick et al. 2005), *Suzaku* (Kubota et al. 2007), *XMM-Newton* (Díaz Trigo et al. 2013), and *NuSTAR* (King et al. 2014). By fitting the *RXTE* spectra taken between 2002 and 2005 with the MCD plus power-law model, Tomsick et al. (2005) suggest that the accretion disk exhibited a state transition between the standard disk and the slim disk at high mass accretion rates. Similar results are also reported by Abe et al. (2005) using the *RXTE* data. Most of these studies, however, apply simple, phenomenological models to the spectra that are limited in the energy resolution or band coverage. To understand the physical conditions of the accretion flow in the VHS, detailed analysis based on physically self-consistent models would be required.

4U 1630–47 is an important target to study the disk wind and jet formation mechanism. Kubota et al. (2007) discover absorption lines from highly ionized iron ions in the *Suzaku* spectra of 4U 1630–47 in the HSS, indicating the presence of disk wind, at least, in this state. Recently, King et al. (2014) also reported an absorption-line feature around 7 keV when the source was in a very similar state to that in the first observation of Kubota et al. (2007). These facts suggest a relatively high inclination angle of the system, $i \sim 70^\circ$, from analogy with other BHBs with disk wind signatures (Ueda et al. 1998; Kotani et al. 2000; Ponti et al. 2012). This is also supported by Muñoz-Darias et al. (2013) from the rather hard color of the disk in the HSS, which can be explained by relativistic effects on the disk spectrum at high inclination. Díaz Trigo et al. (2013) discover Doppler-shifted emission lines of relativistic baryonic jets from an *XMM-Newton* observation performed on 2012 September 28.

In this paper, we analyze the *Suzaku* data of 4U 1630–47 taken in the VHS during the 2012 outburst. The observations and data reduction are described in Section 2. We present the analysis results of the VHS spectra in Section 3. The method to correct for the dust-scattering effects is explained there. The results of reanalysis of the HSS spectra taken in 2006 February are presented in Section 4. We report the results from infrared observations performed one day before the *Suzaku* one at the Infrared Survey Facility (IRSF) in Section 5. Discussions are given in Section 6, focusing on the inner disk truncation, jet lifetime, and disk wind. Throughout the paper, we adopt the distance of $D = 10$ kpc and inclination angle of $i = 70^\circ$ as the reference values. We assume the solar element abundances given by Anders & Grevesse (1989). All errors attached to spectral parameters are those at 90% confidence limits for a single parameter of interest.

## 2. OBSERVATION AND DATA REDUCTION

We performed a Target of Opportunity (ToO) observation of 4U 1630–47 with *Suzaku* from 2012 October 2 00:24:59 (UT) to 20:38:24. Figure 1 shows its long-term light curves in the 3–10 keV and 15–50 keV bands obtained with the Gas Slit Camera (GSC) on board *Monitor of All-sky X-ray Image* (*MAXI*; Matsuoka et al. 2009) and the Burst Alert Telescope (BAT) on board *Swift* (Burrows et al. 2005), respectively. The *MAXI* light curves are obtained by the image-fitting method described in Hiroi et al. (2013). The epoch of the *Suzaku* observation is indicated with the down arrow (left) in Figure 1. As noticed from the figure, it corresponds to the peak of the hard X-ray flux above 15 keV during the 2012 September–October outburst. Detailed behavior in the soft band (<10 keV) was more complex, showing large variability for ~10 days before the *Suzaku* observation. The inset in Figure 1 plots the *MAXI* light curve in 1/4 day bins around the *Suzaku* observation. The data between MJD = 56,199 and 56,200.25 are not available because the source was out of the field of view of *MAXI*. Figure 2 plots the hardness–intensity diagram corresponding to the epoch shown in Figure 1. It first evolved in the opposite direction to the normal track of BHBs in outbursts (Fender et al. 2004), i.e., it moved from left to right along the upper branch of the hardness–intensity diagram. We note that this is a well-known behavior of the VHS in several BHBs (e.g., Tomsick et al. 2005; Motta et al. 2012).

*Suzaku* (Mitsuda et al. 2007) carries two types of instruments, the X-ray Imaging Spectrometer (XIS) and the Hard X-ray Detector (HXD). The XIS is a focal-plane X-ray CCD camera coupled to the X-ray telescope and covers the 0.2–12 keV band. At the time of our observation, two front-side-illuminated XISs (FI-XISs), XIS0 and XIS3, and one back-side-illuminated XIS (BI-XIS), XIS1, were available. The HXD is a collimated-type non-imaging instrument, consisting of silicon PIN diodes and gadolinium silicon oxide (GSO) crystal scintillators, which cover the 10–70 keV and 40–600 keV bands, respectively. To minimize photon pileup events, all XISs were operated with a burst option of 0.1 s exposure per frame. The one fourth window mode was employed for XIS0 and XIS1, while the full window mode was used for XIS3. The net exposure time for XIS0 and XIS1 is ≈3 ks, and that for XIS3 is ≈0.5 ks. The HXD was operated in the standard mode, and its net exposure time corrected for dead time is ~40 ks.

We utilize the "cleaned" event files reduced by the pipeline processing version 2.8.16.34 and analyze them in a standard manner with HEASOFT version 6.12 and Calibration Database released on 2012 September 2. To extract the XIS light curves and spectra, we accumulate photon events in a circular region with a radius of 1.′8 centered at the source position. The background of the XIS is neglected because the contribution is less than 1% of the source counts. As for the background of the HXD, we utilize the so-called tuned background files provided by the *Suzaku* team. The modeled cosmic X-ray background is further subtracted from the PIN data but not from the GSO

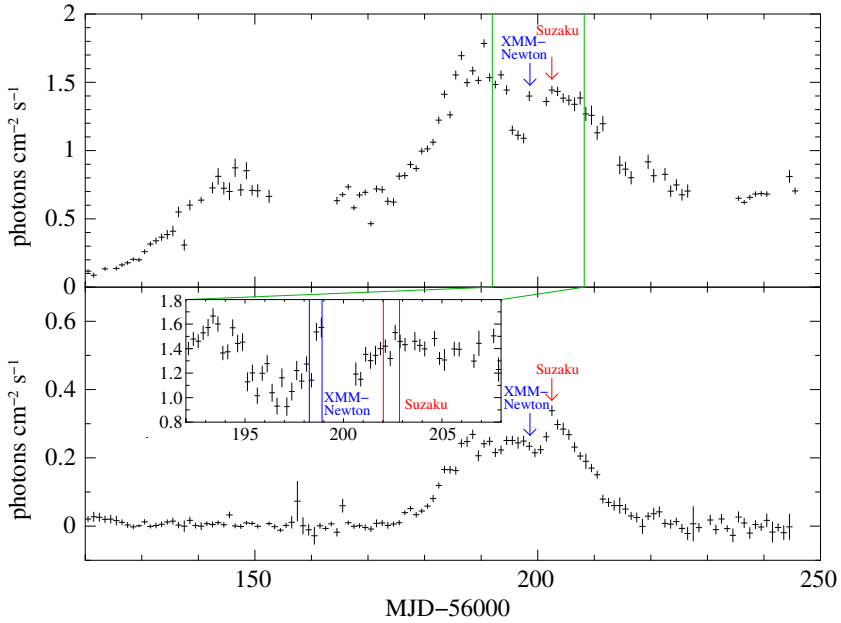


**Figure 1.** Long-term light curves of 4U 1630–47 in the 3–10 keV and 15–50 keV bands obtained with *MAXI*/GSC (top panel) and *Swift*/BAT (bottom panel), respectively. The photon fluxes are converted from the count rates by assuming a power-law photon index of 2.1. The attached error bars correspond to the statistical errors ($1\sigma$) only. Systematic errors of $\sim$10% could be present in the *MAXI*/GSC light curve. The observation epoch by *Suzaku* (this work) and that by *XMM-Newton* (Díaz Trigo et al. 2013) are indicated by the red (right) and blue (left) down arrows, respectively. The inset plots the *MAXI* light curve in one fourth day bins around the *Suzaku* observation. The red and blue lines represent the observation epoch by *Suzaku* and *XMM-Newton*, respectively.

(A color version of this figure is available in the online journal.)

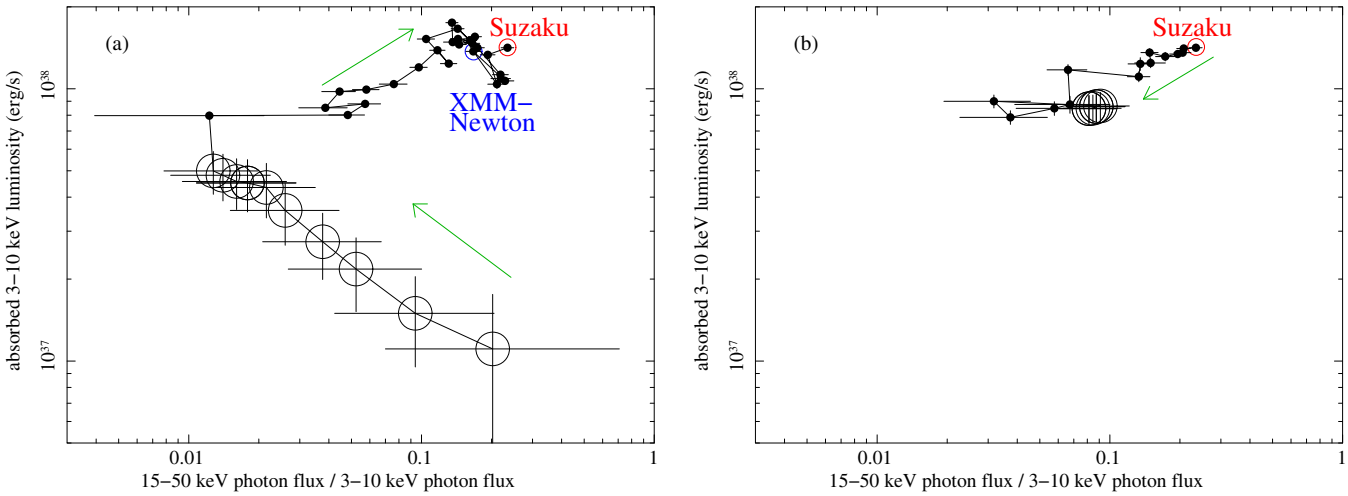


**Figure 2.** Hardness–intensity diagrams using the *MAXI* and *Swift*/BAT light curves shown in Figure 1 (MJD = 56,120–56,250). Panels (a) and (b) correspond to those before and after the *Suzaku* observation, respectively. The epoch of the *XMM-Newton* (*Suzaku*) observation is marked by the blue (red) circle. To reduce the statistical errors, the light curves are binned in five days during MJD = 56,120−56,175 and MJD = 56,220−56,250, whose data points are indicated by the open circles. The other data (MJD = 56,176−56,219) are binned in 1 day, indicated by the small filled circles. Starting from the bottom part in panel (a), it evolves in a clockwise direction, as shown by the green arrows. After the *Suzaku* observation, it moves to the lower left, as shown by the green arrow in panel (b).

(A color version of this figure is available in the online journal.)

data since its contribution is less than 0.1% of the total GSO background.

Figure 3 plots the *Suzaku* light curves of 4U 1630–47 in three energy bands, 2–10 keV (XIS), 10–60 keV (PIN), and 50–200 keV (GSO). The averaged 2–10 keV flux measured by XIS0 is about $1.1 \times 10^{-8}$ erg s$^{-1}$ cm$^{-2}$. The PIN and GSO light curves are corrected for dead time. Figure 4 shows the normalized power spectral density (PSD) obtained from the PIN light curve with 0.025 s binning. This PSD is calculated over the entire observation duration by using the powspec tool in the XRONOS software package version 5.22. As noticed, no significant quasi-periodic oscillation is detected in the range of 0.001–0.02 Hz.

The time-averaged spectra of the XIS and the HXD are plotted in the uppermost panel of Figure 5. We create the response matrix files and auxiliary response files of the XIS with the FTOOL `xisrmfgen` and `xissimarfgen` (Ishisaki et al. 2007), respectively. As for the response file of the HXD, we use `ae_hxd_pinxinome11_20110601.rsp` for PIN and `ae_hxd_gsoxinom_20100524.rsp` and `ae_hxd_gsoxinom_crab_20100526.arf` for GSO. To account for possible calibration uncertainties, 1% systematic errors are included in each

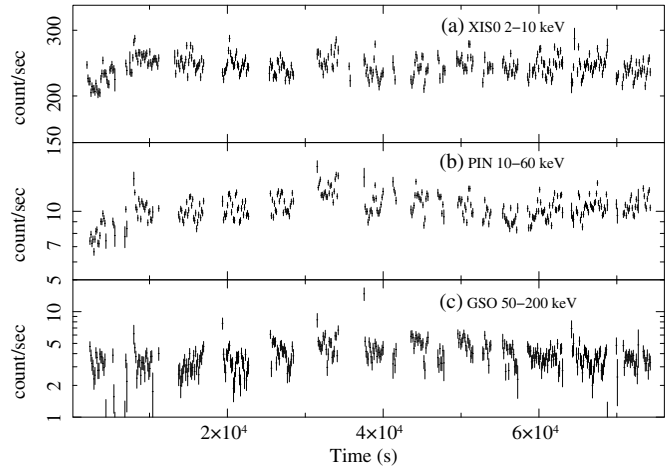


**Figure 3.** *Suzaku* light curves of 4U 1630–47 binned in 128 s obtained with XIS0 in the 2–10 keV band (top panel), HXD/PIN in the 10–60 keV band (middle panel), and HXD/GSO in the 50–200 keV band (bottom panel). The background subtraction and the dead-time correction are applied for the HXD data.

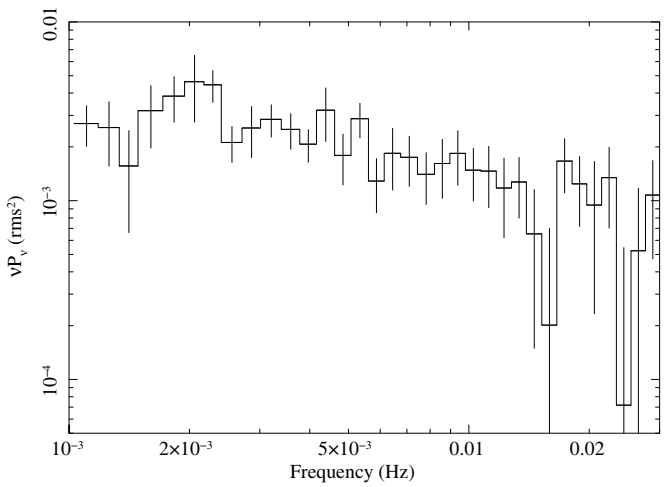


**Figure 4.** Normalized PSD calculated from the HXD/PIN light curve in the 10–60 keV band. The white noise is subtracted.

spectral bin of all spectra. Considering possible calibration uncertainties in the low-energy tail in the pulse height amplitude distribution, we increase the errors to 3% at energies below 1.7 keV in the XIS spectra.

In order to compare our results in the VHS with those in the HSS, we reanalyze the XIS spectra taken between 2006 February 8 15:09:56 and February 9 03:20:18 (ObsID=400010010) published by Kubota et al. (2007). The main reason is to obtain the MCD parameters in the HSS by taking into account dust-scattering effects, which were neglected in Kubota et al. (2007). All XISs were operated with the one fourth window mode and 1 s burst option in this observation. The net exposure is 22 ks for each XIS. The XIS spectra are integrated within a circular region of a radius of 4.′3, while central regions of 30″ are excluded in order to minimize the effect of pileup. The HXD was operated in the standard mode, and its net exposure time corrected for dead time is ∼22 ks. The same systematic errors as those applied for the 2012 data are included. The flux in the 2–10 keV band is about $6.6 \times 10^{-9}$ erg s$^{-1}$ cm$^{-2}$.

## 3. ANALYSIS OF THE TIME-AVERAGED SPECTRA IN THE VHS

In this section, we present the results of detailed spectral analysis of the *Suzaku* data of 2012 October. The spectral fit is performed by using XSPEC version 12.8.0. We simultaneously fit the spectra of three XISs, HXD/PIN, and HXD/GSO, using the energy range of 1.2–9.0 keV for XIS0 and XIS3, 1.2–8.0 keV for XIS1, 13–60 keV for PIN, and 70–200 keV for GSO. The XIS data in the 1.7–1.9 keV energy band were excluded in the spectral fit to avoid the large calibration uncertainties. The cross-normalization factor between XIS0 and HXD (both PIN and GSO) is fixed at 1.164,[9] while those between XIS0, XIS1, and XIS3 are set to be free. We extend the energy range of the spectral fit to 0.01–1000 keV when using convolution models.

### 3.1. Effects by Dust Scattering

Because 4U 1630–47 suffers from heavy absorption ($N_{\rm H} \sim 8 \times 10^{22}$ cm$^{-2}$) by the interstellar medium, we have to take into account the effects by dust scattering, which become more significant at lower energies. A part of the direct emission from the object is scattered out by interstellar dust, while photons emitted toward slightly different angles are scattered in the line of sight, thus making the dust-scattering halo around the point source. When one cannot integrate all the emission including both direct and halo components, the scattered-in and scattered-out photons do not cancel each other. The situation becomes more complex for a variable source because there is a time delay between the scattered-in and direct photons due to their different path lengths. Hence, we have to take into account these effects in the spectral analysis of a heavily absorbed object unless the spectrum is constant and the integrated image region is sufficiently large to fully cover the dust-scattering halo.

Following the work by Ueda et al. (2010), who applied the same procedure to *Suzaku* data of GRS 1915+105, we first estimate the fraction of the dust-scattering halo of 4U 1630-47 contained in our XIS spectra. According to Smith et al. (2002), who studied the detailed image profile of the dust-scattering halo of the bright Galactic source GX 13+1 observed with *Chandra*, the surface density of the halo profile can be approximately represented by a power law with $r^{-1.7}$ below $r = 2.'5$ and $r^{-2.8}$ above $r = 2.'5$. We then run the FTOOL `xissimarfgen` by assuming this profile and find that about 65% of the total photons of the dust-scattering halo are included in the VHS spectra within our integration region. In the spectral fit, we utilize the `Dscat` model, a local model on XSPEC developed by Ueda et al. (2010). It calculates the fractions of the scattered-in and scattered-out components as a function of energy, by referring to the cross section of the dust scattering given by Draine (2003).[10] The free parameters of the `Dscat` model are the hydrogen column density ($N_{\rm H}$) and the fraction of the halo (scattered-in) component contained in the XIS spectra (hereafter "scattering fraction"), which is fixed at 0.65. This is not applied to the spectra of the HXD, which has a sufficiently large field of view. For simplicity, we neglect the effect of time variability. The maximum time delay of the scattered-in component to the direct one is estimated to be ≈1.5 days at the outer integration radius of 1.′8 by assuming that the scatterers are located at the half distance of $D = 10$ kpc. The *MAXI* light curve (Figure 1) shows that the soft X-ray flux was constant within 10% for

[9] http://www.astro.isas.ac.jp/suzaku/doc/suzakumemo/suzakumemo-2008-06.pdf

[10] We adopt that for the Milky Way with $R_{\rm V} = 3.1$.

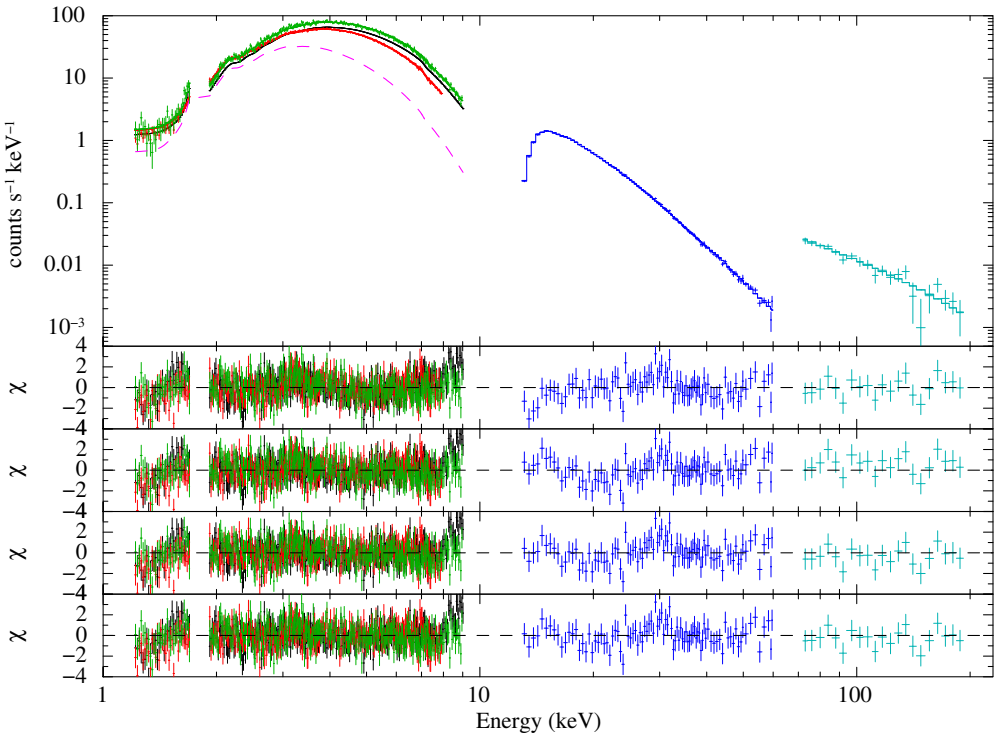


**Figure 5.** Time-averaged spectra of the XIS0 (black), XIS1 (red), XIS3 (green), PIN (blue), and GSO (sky blue) spectra (top panel). The magenta dashed curve indicates the estimated contribution from the dust-scattering halo in XIS0 (see the text). (a)–(d) Residuals between the data and model in units of $\chi$ for Models A, B, C, and D, from upper to lower.

(A color version of this figure is available in the online journal.)

1.5 days before the *Suzaku* observation. We confirm that our conclusions are not affected (see Section 6.2).

In the spectral fit presented below, we add to an intrinsic model both the `wabs` and `Dscat` models, which take into account the interstellar photoelectric absorption (Morrison & McCammon 1983) and dust-scattering effects, respectively. (The hydrogen column density of the `Dscat` model is linked to that of the `wabs` model.) The estimated contribution of the halo component in the XIS0 spectrum is plotted by the magenta curve in the upper limit of Figure 5. We find that the net effects by dust scattering are ≈83% at 2 keV and ≈66% at 3 keV compared with the case when neglected. Thus, consideration of the dust-scattering effects is critical when we discuss the intrinsic source spectrum at low energies.

### 3.2. Simple Models (Model A)

To begin with, we try simple phenomenological models to fit the XIS+HXD spectra in the VHS. We find that a single power-law model gives a very poor fit ($\chi^2$/dof = 4386/1032), with the best-fit photon index of $\Gamma \simeq 3.2$. The model leaves systematic hard X-ray excess above ≈20 keV that monotonically increases with energy and soft excess below ≈2 keV. The residuals indicate that the overall spectral shape is approximated by a power law flatter than $\Gamma \simeq 3.2$, on which an additional soft component is required.

Next, we fit the spectra with an MCD plus a power-law model (`diskbb + pow` in the XSPEC terminology, hereafter referred to as "Model A"). This is a conventional model often adopted to fit the spectra of BHBs in the HSS when a power-law component is rather weak. We find that this model well reproduces the *Suzaku* spectra in the VHS with $\chi^2$/dof = 1266/1030, even though the power-law component dominates the total flux at all energies from 1.2 keV to 200 keV, unlike the case of the HSS. We obtain a power-law photon index of $\Gamma = 2.79^{+0.01}_{-0.02}$ and innermost disk temperature and radius of $T_{\rm in} = 1.41^{+0.02}_{-0.01}$ keV and $r_{\rm in} = (24.8 \pm 0.5)\zeta_{70} d_{10}$ km from the MCD component, where $\zeta_{70} = (\cos i/\cos 70^\circ)^{-1/2}$ and $d_{10} = D/(10\ {\rm kpc})$. The model description and best-fit parameters are given in Tables 1 and 2, respectively. Figure 5(a) shows the residuals between the data and model in units of $\chi$. The best-fit unabsorbed spectrum of Model A is shown in Figure 6(a), where different components are separately plotted. The absorbed 1.2–200 keV flux is estimated to be $1.7 \times 10^{-8}$ erg cm$^{-2}$ s$^{-1}$, which corresponds to the absorbed luminosity of $2.0 \times 10^{38}\ d_{10}$ erg s$^{-1}$ assuming isotropic emission. This high luminosity and the dominant steep power-law component confirm that the object was in the VHS.

### 3.3. Disk and Corona with Reflection (Model B)

Hereafter we apply more physically motivated models, where the power-law component is modeled as Comptonization of seed photons emitted from the disk. Essentially the same models are employed to fit the *Suzaku* spectrum of the BHB GX 339–4 in the VHS by Tamura et al. (2012). First, we utilize the `simpl` model (Steiner et al. 2009) multiplied to the `diskbb` component. The `simpl` model is an empirical model in which a fraction of the photons in an input seed spectrum are Compton-scattered into a power-law component. We find that this model alone does not reproduce the XIS+HXD spectra, yielding $\chi^2$/dof = 1386/1030.

To improve the fit, we further consider the reflection of the Comptonized component from the accretion disk by using the `rfxconv` model (Kolehmainen et al. 2011). This is a convolution model that combines the reflected spectra of Ross & Fabian

**Table 1**
Model Description in XSPEC

| Model | Descriptions in XSPEC |
|---|---|
| Model A[a] | `wabs*Dscat*(diskbb+powerlaw)` |
| Model B[a,b] | `wabs*Dscat*(simpl(D)*diskbb+simpl(C)*diskbb+ rdblur*rfxconv*simpl(C)*diskbb)` |
| Model C[a,b] | `wabs*Dscat*(simpl(D)*diskbb+simpl(C)*diskbb+nthcomp+ rdblur*rfxconv*(simpl(C)*diskbb+nthcomp))` |
| Model D[a,b,c] | `wabs*Dscat*(simpl(D)*dkbbfth(D)+simpl(C)*dkbbfth(D)+dkbbfth(C)+ rdblur*rfxconv*(simpl(C)*dkbbfth(D)+dkbbfth(C)))` |

**Notes.** Energy range is extended to 0.01–1000 keV to use the convolution model.
[a] `Dscat` is a local model, developed by Ueda et al. (2010), to take into account the effect of dust scattering.
[b] `simpl(D)` and `simpl(C)` represent the Direct and the Comptonized component, respectively.
[c] `dkbbfth(D)` and `dkbbfth(C)` represent the disk and Compton components of the `dkbbfth` model, respectively.

**Table 2**
Fitting Results

| Component | Parameter | Model A | Model B | Model C | Model D |
|---|---|---|---|---|---|
| `wabs` | $N_{\rm H}(10^{22}\ {\rm cm}^{-2})$ | $9.38 \pm 0.06$ | $8.32^{+0.07}_{-0.06}$ | $8.46 \pm 0.07$ | $8.39 \pm 0.07$ |
| `diskbb` | $kT_{\rm in}$(keV) | $1.41^{+0.02}_{-0.01}$ | $1.16^{+0.02}_{-0.01}$ | $1.12 \pm 0.02$ | ... |
| | $r_{\rm in}(\zeta_{70} d_{10}\ {\rm km})$[a] | $24.8 \pm 0.5$ | $48.2^{+1.2}_{-1.1}$ | $42.2^{+1.2}_{-1.4}$ | ... |
| `nthcomp` | $kT_{\rm in}^{\rm int}$(keV) | ... | ... | ... | $1.30^{+0.04}_{-0.02}$ |
| or | $\Gamma_{\rm th}$ | ... | ... | $3.01^{+0.05}_{-0.04}$ | $2.89^{+0.05}_{-0.04}$ |
| `dkbbfth` | $kT_{\rm e}$(keV) | ... | ... | $300_{-227}$ | $53^{+10}_{-13}$ |
| | Norm | ... | ... | $1.6^{+0.2}_{-0.3}$ | $0.073^{+0.008}_{-0.014}$ |
| | $r_{\rm tran}(r_{\rm in})$ | ... | ... | ... | $5.5^{+0.8}_{-0.9}$ |
| | Derived $\tau$[b] | ... | ... | $0.08^{+0.22}_{-0.01}$ | $0.41^{+0.12}_{-0.07}$ |
| `PL` | $\Gamma_{\rm PL}$ | $2.79^{+0.01}_{-0.02}$ | $2.83^{+0.02}_{-0.03}$ | (2.1)[c] | (2.1)[c] |
| or | Norm | $21.2 \pm 0.9$ | ... | ... | ... |
| `simpl` | $f_{\rm PL}$ | ... | $0.29^{+0.02}_{-0.05}$ | $0.037^{+0.09}_{-0.07}$ | $0.024^{+0.009}_{-0.015}$ |
| `rfxconv`[d] | $\Omega/2\pi$ | ... | $0.66^{+0.25}_{-0.07}$ | $0.87^{+0.59}_{-0.19}$ | $1.16^{+1.62}_{-0.33}$ |
| | $\log(\xi)$ | ... | $3.30^{+0.06}_{-0.07}$ | $3.70^{+0.15}_{-0.22}$ | $3.30^{+0.05}_{-0.12}$ |
| | $\chi^2$/dof | 1266/1030 | 1231/1028 | 1202/1026 | 1189/1026 |
| Photon flux[e] | $F_{\rm disk+th}^{\rm photon}$ | ... | ... | 21.1 | 21.0 |
| Inner radius[f] | $r_{\rm in}^{*}(\zeta_{70} d_{10}\ {\rm km})$ | ... | ... | $51.5^{+1.6}_{-1.3}$ | $41.0^{+0.7}_{-1.7}$ |

**Notes.** Errors represent 90% confidence limits (statistical errors only). Energy range is extended to 0.01–1000 keV.
[a] Calculated using only `diskbb` normalization.
[b] Calculated using Equation (1) in Tamura et al. (2012).
[c] Fixed in the spectral fitting.
[d] The solar abundances are assumed for all heavy elements. The inclination angle is fixed at 70°. The reflected component is relativistically blurred by `rdblur` with fixed $R_{\rm in}^{\rm rdblur} = 6R_{\rm G}$, $R_{\rm out}^{\rm rdblur} = 10^5 R_{\rm G}$, and $\beta = -3$.
[e] Unabsorbed photon flux of the sum of the disk and thermal Compton component in the range of 0.01–100 keV after excluding the reflected component.
[f] The apparent innermost disk radius is calculated by using Equation (A.1) in Kubota & Makishima (2004) for the slab geometry.

(2005) from a constant density ionized disk with the `ireflect` model (a convolution version of the `pexriv` model; Magdziarz & Zdziarski 1995). To consider general relativistic smearing effect, we utilize the model `rdblur` (Fabian et al. 1989). Following Tamura et al. (2012), we fix the iron abundance to be solar, the inner and outer radius $R_{\rm in} = 6\ R_{\rm g}$, $R_{\rm out} = 10^5\ R_{\rm g}$, and the power-law index of emissivity $\beta = -3$, which are very difficult to determine from the fit. We confirm that other choices of the parameters between $R_{\rm in} = 6\ R_{\rm g}$–$10^2\ R_{\rm g}$ or $R_{\rm out} = 10^3\ R_{\rm g}$–$10^5\ R_{\rm g}$ give almost the same results within the errors.

We refer this model including the disk reflection component as "Model B," whose description in the XSPEC terminology is given in Table 1. We find that Model B gives a much better fit with $\chi^2/{\rm dof} = 1231/1028$ than that without a reflection component. The best-fit parameters are summarized in Table 2. The fitting residuals and unabsorbed best-fit model are plotted in Figures 5(b) and 6(b), respectively.

### *3.4. Two Comptonization Components: Thermal and Nonthermal (Model C)*

The `simpl` model used in Model B assumes no high energy cutoff, and hence should be regarded to represent Comptonized emission by nonthermal electrons. However, previous studies of BHBs in the VHS suggest that the Comptonizing corona contains both thermal and nonthermal electrons (e.g., Gierliński et al. 1999; Kubota et al. 2001; Gierliński & Done 2003). It is not clear whether it consists of two separate components or is a

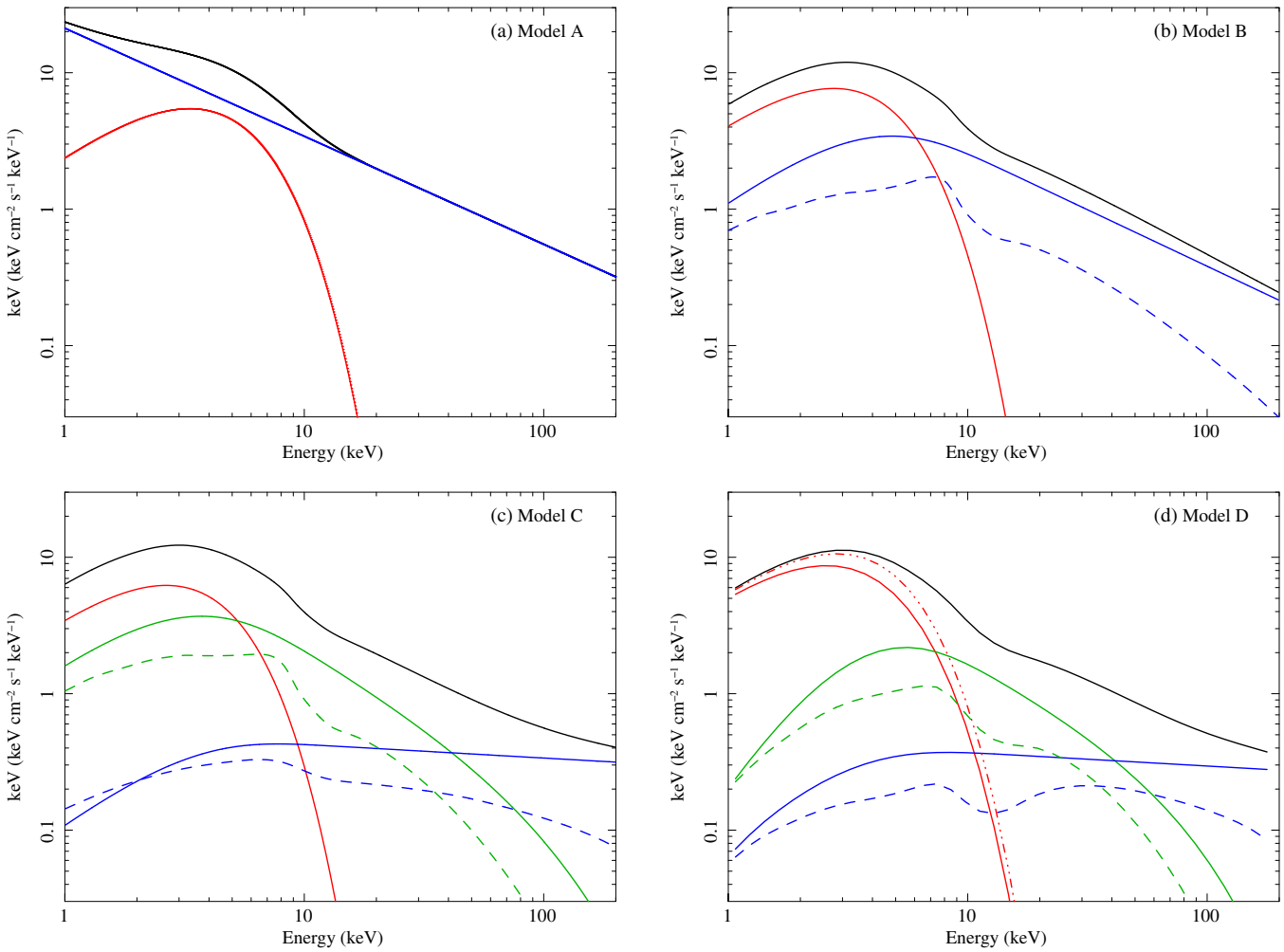


**Figure 6.** Best-fit model spectra corrected for the interstellar absorption in units of $EF(E)$, where $E$ is the energy and $F(E)$ is the energy flux, for Model A (a), Model B (b), Model C (c), and Model D (d). The observed disk component (`diskbb` or `dkbbfth`; red), nonthermal Compton component (`powerlaw` or `simpl(C)`; blue), and thermal Compton component (`nthcomp` or `dkbbfth(C)`; green) are separately plotted with the solid curves. The reflected nonthermal (blue) and thermal (green) Compton component are shown with the dashed curves. In panel (d), we also plot the intrinsic continuum (red dash–dotted line) that would be observed when all the luminosity of the `dkbbfth` component were emitted as the standard disk.

(A color version of this figure is available in the online journal.)

hybrid plasma whose energy distribution is Maxwellian at low energies but a power law at high energies. For simplicity, here we consider the former case and leave the detailed modeling of Comptonization by a hybrid plasma for future work. We note, however, that while a hybrid electron distribution can fit the spectrum, such a homogeneous source model cannot explain the result by Axelsson et al. (2014), who show that the spectrum of the fastest variability is different to that of the time-averaged spectrum. Accordingly, we add a thermal Comptonization model (Zdziarski et al. 1996; Życki et al. 1999) (Model C in Table 1) to Model B. As in Model B, we include the disk reflection component of the Comptonized emission (both thermal and nonthermal ones).

The `nthcomp` model has four parameters, the seed photon temperature, which we tie at the disk temperature of `diskbb`, the electron temperature, the photon index $\Gamma_{\rm th}$, and its normalization. We set the upper limit of the electron temperature to be 300 keV, as the `nthcomp` model does not include full relativistic corrections. Since we cannot constrain both $\Gamma_{\rm th}$ in `nthcomp` and $\Gamma_{\rm pl}$ in `simpl`, we fix $\Gamma_{\rm pl} = 2.1$, a typical value for a nonthermal power-law component seen in the HSS (Gierliński et al. 1999). We note that the choice of $\Gamma_{\rm pl}$ is not sensitive to the overall fitting result as our data is available up to only 200 keV.

In the `nthcomp` model, the relation among the optical depth of corona, the electron temperature, and the photon index is given by Equation (1) of Tamura et al. (2012)

$$\tau = \frac{1}{2}\cdot\left[\sqrt{\frac{9}{4}+\frac{3}{\Theta_{\rm e}\cdot\left(\left(\Gamma_{\rm th}+\frac{1}{2}\right)^2-\frac{9}{4}\right)}}-\frac{3}{2}\right], \quad (1)$$

where $\Theta_{\rm e} = kT_{\rm e}/m_{\rm e}c^2$. It is derived from Equation (A1) of Zdziarski et al. (1996) by assuming a slab geometry. We cannot directly estimate the innermost disk radius using the `diskbb` normalization alone, since the `nthcomp` model does not conserve the photon number unlike `simpl`. We therefore use Equation (A1) of Kubota & Makishima (2004),

$$F^{\rm photon}_{\rm dkbbfth} = 0.0165\left[\frac{r_{\rm in}^2\cos i}{(D/10\ {\rm kpc})^2}\right]\left(\frac{T_{\rm in}}{1\ {\rm keV}}\right)^3 \ {\rm photons\ s^{-1}\ cm^{-2}}, \quad (2)$$

to derive the true innermost radius by considering the photon-number conservation. Note that we replace "$F^{\rm p}_{\rm disk} + F^{\rm p}_{\rm thc} 2\cos i$" in Equation (A1) of Kubota & Makishima (2004) with $F^{\rm photon}_{\rm dkbbfth}$ to assume the slab corona geometry.

We find that Model C gives a better fit than Model B, yielding $\chi^2$/dof = 1202/1026. The improvement from Model B is significant at 99.9995% level from an $F$ test, i.e., the data require the presence of another Comptonized component at high confidence, although the electron temperature of the `nthcomp` component is not well constrained, with a lower limit of 73 keV. The best-fit parameters are summarized in Table 2. Figure 5(c) plots the residuals, while Figure 6(c) shows the unabsorbed best-fit model spectrum. It is seen that the thermal Compton component dominates below ∼50 keV.

### 3.5. Inner Disk–Corona Coupling (Model D)

In reality, it is expected that the hot Comptonizing corona surrounds only an inner part of the disk. In this picture, Model C is unphysical because it does not take into account any energetic coupling between the disk and corona; the summed emissivity of the disk blackbody and thermal Comptonization components in an inner region is larger than the extrapolation from the outer disk that is not Comptonized (see Done & Kubota 2006; Tamura et al. 2012). This would lead an incorrect estimate of the innermost disk radius. To overcome this situation, we replace `diskbb` and `nthcomp` to `dkbbfth` (Done & Kubota 2006) (Model D in Table 1). The `dkbbfth` model assumes that the energy released by gravity is dissipated locally, which is emitted purely from the standard disk at $r > r_{\rm tran}$ but is split into the disk and corona at $r_{\rm in} < r < r_{\rm tran}$. Thus, the inner part of the disk covered by the corona is less luminous than it would have been if the corona did not exist. The `dkbbfth` model has five parameters, the disk temperature, the outer radius of the corona $r_{\rm tran}$, the photon index of the Comptonized component, the temperature of the corona, and the normalization. We set all these parameters to be free in the fitting. Since this model only takes into account thermal Comptonization, we further add the `simpl` model to describe nonthermal Comptonization. There we set the disk emission to be the seed photons of `simpl` and fix the photon index at 2.1. We note that the number of free parameters in Model D is the same as in Model C.

The fit shows a significant improvement ($\chi^2$/dof = 1189/1026) from Model C. Thus, we conclude that Model D gives the best description of the *Suzaku* spectra among the three physically motivated models examined above. The best-fit parameters are summarized in Table 2 and the fitting residuals are plotted Figure 5(d). The best-fit unabsorbed model is shown in Figure 6(d). The dash–dotted curve shows the intrinsic disk emission that would be observed when all the luminosity of the `dkbbfth` component were emitted as the standard disk.

## 4. REANALYSIS OF XIS SPECTRA IN THE HSS

To compare with the results in the VHS, we also perform spectral fit to the *Suzaku* spectra of 4U 1630–47 taken in 2006 February 8 when the object was in the HSS (see Section 2). We simultaneously fit the spectra of the four XISs and HXD/PIN. We utilize the energy band of 13–30 keV of the PIN spectrum. Only the XIS spectra below 6 keV are utilized to avoid pile-up effects that produce an artificial hard excess above ∼7 keV and to ignore the strong absorption lines from highly ionized iron ions (see Kubota et al. 2007 for details). The energy ranges of 1.7–1.9 keV and 2.2–2.4 keV are excluded, where calibration uncertainties are large. Systematic errors of 1% and 3% are included in each spectral bin above 1.9 keV and below 1.7 keV, respectively. In the same way as for the VHS spectra, we add the `Dscat*wabs` model to the intrinsic continuum to take into account dust-scattering effects, which could affect the continuum spectral parameters reported by Kubota et al. (2007). Using the `xissimargen` FTOOL, we estimate the scattering fraction to be 0.78. The cross-normalization factor of HXD/PIN relative to XIS0 is fixed at 1.164, while those of XIS1, XIS2, and XIS3 are set to be free. Thus, we can directly compare the absolute flux between the two states by using the XIS0 as the reference.

We apply a model consisting of the MCD component and its Comptonization (`simpl*diskbb` in the XSPEC terminology). The photon index in `simpl` is fixed at 2.1 (see Figure 2(b) of Kubota et al. 2007). Although the model is rather simple, the fit is found to be reasonably good with $\chi^2$/dof = 1740/1438. We obtain the innermost disk temperature and radius of $T_{\rm in} = 1.31 \pm 0.01$ keV and $r_{\rm in} = (35.0 \pm 0.3)\zeta_{70} d_{10}$ km, respectively. The derived innermost radius is larger than that reported by Kubota et al. (2007), $r_{\rm in} \simeq 25\zeta_{70} d_{10}$ km. The difference is attributable to the dust-scattering effects. The hydrogen column density is determined to be $N_{\rm H} = (8.30^{+0.03}_{-0.02}) \times 10^{22}$ cm$^{-2}$, which is consistent with the Kubota et al. (2007) result and our result in the VHS. The small scattered fraction $f_{\rm PL} = 0.0048 \pm 0.0002$ means that the MCD component was dominant in this observation. The absorbed 1.2–30 keV flux is estimated to be $6.9 \times 10^{-9}$ erg s$^{-1}$ cm$^{-2}$, which gives an absorbed luminosity of $8.3 \times 10^{37}$ erg s$^{-1}$ by assuming isotropic emission.

## 5. NEAR-INFRARED OBSERVATION AND RESULTS IN THE VHS

### 5.1. Observation and Data Reduction

We performed near-infrared photometric observations of 4U 1630–47 in the $J$ (1.25 $\mu$m), $H$ (1.63 $\mu$m), and $K_{\rm s}$ (2.14 $\mu$m) bands on 2012 October 1 (one day before the *Suzaku* observation) by using the SIRIUS camera (Nagayama et al. 2003) on the 1.4 m IRSF telescope at the South African Astronomical Observatory. We obtained 25 object frames with an exposure of 15 s per frame, and thus the net exposure time was 375 s. The seeing in FWHM in the $J$ band was ∼1.″5 (3.5 pixels).

We perform standard data reduction (i.e., dark subtraction, flat-fielding, sky subtraction, and combining dithered images) with the IRSF pipeline software on IRAF (the Image Reduction and Analysis Facility, distributed by the National Optical Astronomy Observatory), version 2.16. We combine all the object frames obtained in one night to maximize signal-to-noise ratio.

The near-infrared counterpart has been identified by Augusteijn et al. (2001), but we are not able to measure the flux by aperture photometry since 4U 1630–47 is contaminated by nearby stars in the infrared images. Thus, we perform point-spread functionphotometry using the DAOPHOT (Stetson 1987) package in IRAF.

### 5.2. Results

We obtain the near-infrared magnitudes of 17.9 ± 0.4 mag in the $H$ band and 16.0 ± 0.2 mag in the $K_{\rm s}$ band, while we are unable to constrain the $J$-band flux because of the severe source confusion. These magnitudes are almost the same as those reported in the 1998 outburst (Augusteijn et al. 2001). We estimate the extinction in each band as $A_H = 7.8 \pm 1.3$ mag and $A_K = 5.0 \pm 0.9$ mag by using the relation between the hydrogen column density and optical extinction $A_V$, $N_{\rm H} = (1.79 \pm 0.03) \times A_V$[mag] $\times 10^{21}$[cm$^{-2}$] (Predehl & Schmitt 1995), and the conversion factor from $A_V$ into $A_H$ or $A_K$ given by Rieke & Lebofsky (1985). The extinction-corrected IRSF

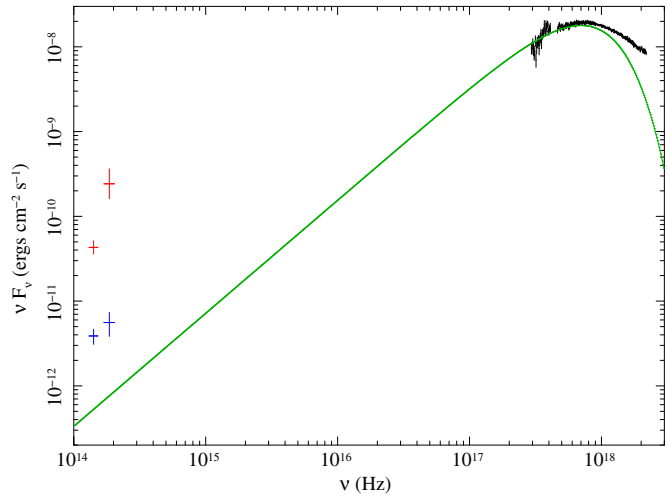


**Figure 7.** Spectral energy distribution of 4U 1630–47 in the VHS. The red points correspond to the absorption-corrected fluxes in the $H$ (1.63 $\mu$m) and $K_s$ (2.14 $\mu$m) bands obtained on 2012 October 1. These fluxes have an extremely blue color, which may indicate that the absorption correction is overestimated. More moderate absorption-corrected fluxes using the half of $N_{\rm H}/A_V$ conversion factor are also plotted in the blue color. The exact fluxes must be located between the red points and the blue points. The black data are the XIS0 spectrum. The green curve represents the intrinsic `diskbb` emission that would be observed without Comptonization in Model D. Note that this does not match the total observed fluxes because of the Comptonization. All data are corrected for the interstellar extinction or absorption.

(A color version of this figure is available in the online journal.)

fluxes ($m_H^{\rm cor} = 10.1$ mag, $m_K^{\rm cor} = 11.0$ mag) are plotted as the red points in Figure 7. Note that the extremely blue color ($m_H^{\rm cor} - m_K^{\rm cor} = -0.9$ mag), which is hard to explain by any stellar or continuum source, most probably comes from the errors in the photometry, $N_{\rm H}$, and/or the $N_{\rm H}$-to-$A_V$ conversion. We find that the last one can produce the largest uncertainty. Figure 3 of Predehl & Schmitt (1995) shows that there is a deviation by a factor of ∼two in the relation between $N_{\rm H}$ and $A_V$ for some objects. Accordingly, we consider an extreme case where the $A_V$-to-$N_{\rm H}$ ratio is twice smaller than the above as a lower limit of the extinction correction. This gives the corrected fluxes of $m_H^{\rm cor} = 13.8$ mag and $m_K^{\rm cor} = 13.4$ mag, which are plotted as the blue points in Figure 7. Thus, the extinction-corrected magnitudes are estimated to be in the range of 13.8 mag $> m_H^{\rm cor} > 10.1$ mag and 13.4 mag $> m_K^{\rm cor} > 11.0$ mag.

In Figure 7, the intrinsic thermal emission from the standard disk based on Model D (Section 3.5) that would be observed without Comptonization (i.e., the red dashed line in Figure 6(d)) is plotted by the green solid curve. As noticed, even the lower limits of the observed near-infrared fluxes are larger than the expected fluxes from the MCD component. This suggests that the fluxes are dominated by other components. We estimate the absolute magnitudes to be $-1.2$ mag $> M_H^{\rm cor} > -5.3$ mag and $-1.6$ mag $> M_K^{\rm cor} > -4.2$ mag for a distance of 10 kpc. Thus, if the near-infrared fluxes completely come from the companion star, it would be an early-type star (O7–B2), supporting the suggestion by Augusteijn et al. (2001), or a K-type giant star.

These magnitudes should be regarded as the upper limit of the true luminosity of the companion star, however, as we also expect other origins that could be responsible for the near-infrared fluxes, including (1) the irradiation of the outer disk by the X-ray emission, (2) synchrotron radiation from the jets, and/or (3) cyclo-synchrotron emission from the hot flow (Veledina et al. 2013). Unfortunately, the large uncertainties in the extinction-corrected fluxes make it very difficult to discriminate these possibilities. We note that the observed (uncorrected) near-infrared fluxes in the VHS are almost the same as those reported by Augusteijn et al. (2001) when the source was in the HSS with a similar X-ray flux level. Since jet ejection is believed to be quenched in the HSS, this comparison suggests that the synchrotron emission from the jets, if any, is not a dominant source of the near-infrared fluxes in the VHS.

## 6. DISCUSSIONS

### 6.1. Result Summary

Using *Suzaku*, we have obtained so far the best-quality broadband X-ray spectra of 4U 1630–47 in the VHS, covering the 1–200 keV band with good energy resolution by X-ray CCD below 10 keV. The observation epoch corresponds to when the hard X-ray flux above 15 keV was peaked during the 2012 September–October outburst. In the spectral analysis, we carefully take into account the effects by dust scattering.

The continuum is found to be well approximated by a phenomenological model consisting of an MCD and a power-law component dominating the total flux in the entire 1.2–200 keV band (Model A). However, we regard that this modeling is unnatural because (1) no low-energy turnover is included, which should exist if the power-law component is originated by Comptonization of seed photons emitted from the disk, and (2) the derived column density is significantly larger than that obtained in the HSS. We thus consider three physically motivated models where the disk photons are Compton-scattered by a hot corona surrounding it. Among them, Model D, where the Comptonizing corona is energetically coupled with the underlying standard disk below a transition radius, best reproduces the spectra. A significant reflection component from the inner disk with a solid angle of $\Omega/2\pi \approx 1.2$ is detected. This is consistent with the recent result by King et al. (2014), although the state was different from ours. Below, we discuss the inner disk geometry on the basis of the result of Model D. No significant emission or absorption lines are detected in our spectra. This fact gives tight constraints on the presence of the baryonic jets discovered by Díaz Trigo et al. (2013) four days before the *Suzaku* observation and that of the disk wind seen in the HSS (Kubota et al. 2007; King et al. 2014).

### 6.2. Inner Disk Truncation in the VHS

We find that the standard disk in the VHS is most likely truncated before reaching the ISCO. From Model D, the best physically self-consistent model considered here, we derive the innermost radius of the standard disk as $r_{\rm in} = 41.0^{+0.7}_{-1.7}\zeta_{70}d_{10}$ km in the VHS. This is significantly larger than that found in the HSS, $r_{\rm in} = (35.0 \pm 0.3)\zeta_{70}d_{10}$ km, which is found to be constant during this state and hence most probably corresponds to the ISCO (Kubota et al. 2007). Since we directly compare the results obtained with the same detector (XIS0), the comparison is free from any cross-normalization uncertainties between different instruments. Also, a common model is employed to represent the interstellar absorption and dust scattering, making the relative systematic error least. When we assume an extreme case in which the soft X-ray flux producing the dust-scattering halo is 10% lower than the *Suzaku* epoch (see Section 3.1), we obtain an even larger innermost radius. Thus, the conclusion of disk truncation is robust against uncertainty in the correction for dust scattering.

A truncated disk in the VHS is also suggested from the BHB GX 339–4 by applying essentially the same model as our Model D (Tamura et al. 2012). Hence, disk truncation would be a common feature of the VHS, although the innermost radius is less than twice that of the ISCO in both objects. We note that the "true" disk radius, $R_{\rm in}$, is estimated as $R_{\rm in} = \kappa \xi^2 r_{\rm in}$, where $\kappa$ is the color-to-effective temperature ratio and $\xi$ is a correction factor for the stress-free boundary condition at the ISCO (Kubota et al. 1998). To explain the $r_{\rm in}$ value in the VHS by the ISCO, $\kappa$ must be smaller than that in the HSS. As discussed in Tamura et al. (2012), this case is quite unlikely under strong irradiation by the corona in the VHS.

### 6.3. Lifetime of Baryonic Jets

Relativistic baryonic jets of 4U 1630–47 were detected with *XMM-Newton* on 2012 September 28 (Díaz Trigo et al. 2013) when the source was also in the VHS. The *XMM-Newton* spectrum shows Doppler-shifted Fe XXVI lines at 7.3 keV and 4 keV. Assuming that they are twin jets of the same physical parameters emitted to opposite directions, they estimate the jet speed, the inclination angle, and the cone angle to be 0.3–0.4$c$, 58°–67°, and 3.°7–4.°5, respectively. The parameters are quite similar to those of SS 433 (Namiki et al. 2003), the unique Galactic microquasar exhibiting steady relativistic jets with a velocity of 0.26$c$, which most likely contains a black hole (Kubota et al. 2010).

In contrast, our *Suzaku* spectra, taken only four days after the *XMM-Newton* observation, do not show such emission-line features. The equivalent width of the 7.3 keV emission line detected by Díaz Trigo et al. (2013) is constrained to be <3 eV (90% confidence limit), which is about 1/12 of that in the *XMM-Newton* spectra. This suggests that the relativistic jets detected by Díaz Trigo et al. (2013) had vanished in four days. In the case of SS 433, the length of the X-ray-emitting region of the jets is $\sim 10^{13}$ cm, corresponding to a traveling time of only $\sim 10^3$ s (Kotani et al. 1996). Thus, if we assume conditions similar to those in SS 433, the jets of 4U 1630–47 would vanish in an hour after the ejection stops. We cannot, however, exclude the possibility that a jet might still exist, such as compact jets often seen in the LHS (Fender et al. 2004).

The variation of the X-ray flux can provide clues to reveal the condition for the ejection of baryonic jets from a black hole. According to the *MAXI* and *Swift*/BAT light curves (Figure 1), the *Suzaku* observation was performed just after the hard X-ray flux showed a sudden increase from MJD≃56,201. The same trend is confirmed in the soft band, though less clear because of the data gap of *MAXI*. The source was by ∼30% fainter when the jets were detected with *XMM-Newton* (MJD = 56,198) than in the *Suzaku* epoch (MJD = 56,202). Thus, phenomenologically, it would be possible that the launch of the baryonic jets somehow ceased as more accretion power was dissipated into radiation. However, we estimate the kinetic power of the jets to be $>10^{40}$ erg s$^{-1}$ on the basis of the jet model of SS 433 (Kotani et al. 1996), assuming that it is proportional to the luminosity of the ionized iron-K emission lines. This huge power cannot be accounted for by the observed increase in the luminosity at MJD≃56,201 ($\Delta L_{\rm X} \sim 10^{38}$ erg s$^{-1}$) unless the radiation efficiency is very low. Thus, a significant decrease in the intrinsic mass accretion rate would be required. To obtain firm observational clues on the jet formation mechanism, we need more frequent monitoring observations of BHBs in high-luminosity states with high-quality X-ray spectroscopy.

### 6.4. Disk Wind in the VHS

The *Suzaku* spectra of 4U 1630–47 in the VHS do not show any significant absorption-line features of highly ionized iron ions that were detected in the HSS by Kubota et al. (2007). The upper limits for the equivalent widths of the absorption lines are 1.3 eV and 1.4 eV (90% confidence limits) at 6.72 keV and 6.99 keV, corresponding to those of Fe XXV and Fe XXVI observed in the HSS, respectively. There are two possibilities to account for this fact: (1) there is actually no disk wind in the VHS, or (2) it exists but simply becomes invisible by being almost fully ionized by the strong X-ray irradiation.

To examine the latter possibility, we perform simulations of a photoionized gas using XSTAR version 2.2.1bk. Following Kubota et al. (2007), we first reproduce the physical parameters (the ionization stage and column density) of the disk wind detected in the HSS by assuming the same spectrum and luminosity as observed. Then, we change the X-ray spectrum and luminosity to those in the VHS by keeping the other parameters the same. We find that the ion fractions of Fe XXV and Fe XXVI become ≈1/20 and ≈1/4 of those in the HSS, respectively. The predicted equivalent width of Fe XXVI is larger than the observed upper limit, suggesting that photoionization effects alone cannot explain the absence of the absorption lines in the *Suzaku* spectra. However, it is still plausible that a disk wind with a smaller density (and/or at a smaller distance) than that in the HSS is present in the VHS (see Chakravorty et al. 2013 for discussion of thermodynamical stability, and Begelman et al. 1983 for discussion of launch radius and density). Further observations of BHBs with good energy resolution covering different states and luminosities are necessary to establish the critical conditions to launch a disk wind.

### 6.5. Conclusion

We observed 4U 1630–47 in the VHS with *Suzaku* and IRSF during the 2012 September–October outburst.

The conclusions are summarized as follows.

1. The time-averaged *Suzaku* spectra are well described by a physically self-consistent model consisting of thermal and nonthermal Comptonization of the inner disk emission with energetic coupling between the disk and corona. A strong relativistic reflection component from the accretion disk is required. We properly take into account the effects of dust scattering.
2. Comparing the result of the *Suzaku* spectra in the HSS observed in 2006 February, we find evidence that the accretion disk is slightly truncated before reaching the ISCO in the VHS.
3. Our spectra do not show any Doppler-shifted line emissions from the relativistic jets that were detected four days before our observation with *XMM-Newton*. This suggests that the jets were a transient event and vanished between these observations.
4. We do not detect absorption-line features from highly ionized iron ions that were previously present in the high/soft state. The upper limits on the equivalent width of these lines are not compatible with over-ionization by the higher luminosity irradiation of the same wind. If a wind still remains, it has changed in launch radius and/or density from that seen in the HSS.
5. From near-infrared data taken with IRSF one day before the *Suzaku* observation, we obtain 17.9 ± 0.4 mag in the $H$ band and 16.0 ± 0.2 mag in the $K_{\rm s}$ band for the

counterpart. Since the extinction-corrected fluxes are larger than the extrapolated fluxes from the MCD component, contribution from a companion star, which would be an early-type star or a K-type giant star if it dominates the total fluxes, and/or other origins such as irradiation of the outer disk by the X-ray emission are required.

We are grateful to the *Suzaku* project for performing this ToO observation upon our request. We thank Tatsuhito Yoshikawa for his help on the analysis of the IRSF data, and Shin'ya Yamada and Shin Mineshige for discussions. This work was partly supported by the Grant-in-Aid for Scientific Research No. 26400228 (Y.U.), No. 24111717 (K.T.), and for young researchers (M.S.).

## REFERENCES

Abe, Y., Fukazawa, Y., Kubota, A., Kasama, D., & Makishima, K. 2005, PASJ, 57, 629
Anders, E., & Grevesse, N. 1989, GeCoA, 53, 197
Augusteijn, T., Kuulkers, E., & van Kerkwijk, M. H. 2001, A&A, 375, 447
Axelsson, M., Done, C., & Hjalmarsdotter, L. 2014, MNRAS, 438, 657
Begelman, M. C., McKee, C. F., & Shields, G. A. 1983, ApJ, 271, 70
Burrows, D. N., Hill, J. E., Nousek, J. A., et al. 2005, SSRv, 120, 165
Chakravorty, S., Lee, J. C., & Neilsen, J. 2013, MNRAS, 436, 560
Díaz Trigo, M., Miller-Jones, J. C. A., Migliari, S., Broderick, J. W., & Tzioumis, T. 2013, Natur, 504, 260
Done, C., Gierliński, M., & Kubota, A. 2007, A&ARv, 15, 1
Done, C., & Kubota, A. 2006, MNRAS, 371, 1216
Draine, B. T. 2003, ApJ, 598, 1026
Ebisawa, K., Makino, F., Mitsuda, K., et al. 1993, ApJ, 403, 684
Esin, A. A., McClintock, J. E., & Narayan, R. 1997, ApJ, 489, 865
Fabian, A. C., Rees, M. J., Stella, L., & White, N. E. 1989, MNRAS, 238, 729
Fender, R. P., Belloni, T. M., & Gallo, E. 2004, MNRAS, 355, 1105
Gierliński, M., & Done, C. 2003, MNRAS, 342, 1083
Gierliński, M., Zdziarski, A. A., Poutanen, J., et al. 1999, MNRAS, 309, 496
Gladstone, J., Done, C., & Gierliński, M. 2007, MNRAS, 378, 13
Hiroi, K., Ueda, Y., Hayashida, M., et al. 2013, ApJS, 207, 36
Ishisaki, Y., Maeda, Y., Fujimoto, R., et al. 2007, PASJ, 59, 113
King, A. L., Walton, D. J., Miller, J. M., et al. 2014, ApJL, 784, L2
Kolehmainen, M., Done, C., & Díaz Trigo, M. 2011, MNRAS, 416, 311
Kotani, T., Ebisawa, K., Dotani, T., et al. 2000, ApJ, 539, 413
Kotani, T., Kawai, N., Matsuoka, M., & Brinkmann, W. 1996, PASJ, 48, 619
Kubota, A., & Done, C. 2004, MNRAS, 353, 980
Kubota, A., Dotani, T., Cottam, J., et al. 2007, PASJ, 59, 185
Kubota, A., & Makishima, K. 2004, ApJ, 601, 428
Kubota, A., Makishima, K., & Ebisawa, K. 2001, ApJL, 560, L147
Kubota, A., Tanaka, Y., Makishima, K., et al. 1998, PASJ, 50, 667
Kubota, K., Ueda, Y., Fabrika, S., et al. 2010, ApJ, 709, 1374
Kuulkers, E., Wijnands, R., Belloni, T., et al. 1998, ApJ, 494, 753
Magdziarz, P., & Zdziarski, A. A. 1995, MNRAS, 273, 837
Makishima, K., Maejima, Y., Mitsuda, K., et al. 1986, ApJ, 308, 635
Makishima, K., Takahashi, H., Yamada, S., et al. 2008, PASJ, 60, 585
Matsuoka, M., Kawasaki, K., Ueno, S., et al. 2009, PASJ, 61, 999
Mitsuda, K., Bautz, M., Inoue, H., et al. 2007, PASJ, 59, 1
Mitsuda, K., Inoue, H., Koyama, K., et al. 1984, PASJ, 36, 741
Morrison, R., & McCammon, D. 1983, ApJ, 270, 119
Motta, S., Homan, J., Muñoz Darias, T., et al. 2012, MNRAS, 427, 595
Muñoz-Darias, T., Coriat, M., Plant, D. S., et al. 2013, MNRAS, 432, 1330
Nagayama, T., Nagashima, C., Nakajima, Y., et al. 2003, Proc. SPIE, 4841, 459
Nakahira, S., Negoro, H., Shidatsu, M., et al. 2014, PASJ, submitted (arXiv:1406.0613)
Namiki, M., Kawai, N., Kotani, T., & Makishima, K. 2003, PASJ, 55, 281
Oosterbroek, T., Parmar, A. N., Kuulkers, E., et al. 1998, A&A, 340, 431
Parmar, A. N., Stella, L., & White, N. E. 1986, ApJ, 304, 664
Parmar, A. N., Williams, O. R., Kuulkers, E., Angelini, L., & White, N. E. 1997, A&A, 319, 855
Ponti, G., Fender, R. P., Begelman, M. C., et al. 2012, MNRAS, 422, L11
Predehl, P., & Schmitt, J. H. M. M. 1995, A&A, 293, 889
Rieke, G. H., & Lebofsky, M. J. 1985, ApJ, 288, 618
Ross, R. R., & Fabian, A. C. 2005, MNRAS, 358, 211
Shidatsu, M., Ueda, Y., Nakahira, S., et al. 2013, ApJ, 779, 26
Shidatsu, M., Ueda, Y., Tazaki, F., et al. 2011, PASJ, 63, 785
Smith, R. K., Edgar, R. J., & Shafer, R. A. 2002, ApJ, 581, 562
Steiner, J. F., Narayan, R., McClintock, J. E., & Ebisawa, K. 2009, PASP, 121, 1279
Stetson, P. B. 1987, PASP, 99, 191
Tamura, M., Kubota, A., Yamada, S., et al. 2012, ApJ, 753, 65
Tomsick, J. A., Corbel, S., Goldwurm, A., & Kaaret, P. 2005, ApJ, 630, 413
Tomsick, J. A., & Kaaret, P. 2000, ApJ, 537, 448
Tomsick, J. A., Lapshov, I., & Kaaret, P. 1998, ApJ, 494, 747
Tomsick, J. A., Yamaoka, K., Corbel, S., et al. 2009, ApJL, 707, L87
Trudolyubov, S. P., Borozdin, K. N., & Priedhorsky, W. C. 2001, MNRAS, 322, 309
Ueda, Y., Honda, K., Takahashi, H., et al. 2010, ApJ, 713, 257
Ueda, Y., Inoue, H., Tanaka, Y., et al. 1998, ApJ, 492, 782
Veledina, A., Poutanen, J., & Vurm, I. 2013, MNRAS, 430, 3196
Zdziarski, A. A., Johnson, W. N., & Magdziarz, P. 1996, MNRAS, 283, 193
Zdziarski, A. A., Poutanen, J., Paciesas, W. S., & Wen, L. 2002, ApJ, 578, 357
Życki, P. T., Done, C., & Smith, D. A. 1999, MNRAS, 309, 561